Appl. Phys. A (2017) 123:763
DOI 10.1007/s00339-017-1390-7

Applied Physics A
Materials Science & Processing

Characterization and magnetic properties study for magnetite nanoparticles obtained by pulsed laser ablation in water

V. A. Svetlichnyi[1] · A. V. Shabalina[1] · I. N. Lapin[1] · D. A. Goncharova[1] · D. A. Velikanov[2] · A. E. Sokolov[2]

Received: 22 August 2017 / Accepted: 7 November 2017 / Published online: 11 November 2017

Abstract Magnetite (Fe_3O_4) nanoparticles of 1–10 nm (with the maximum at 2 nm) were obtained via pulsed laser ablation of iron target in water in form of a stable dispersion without addition of surfactants and stabilizers. The structure of the material obtained was investigated using transmission electron microscopy, scanning electron microscopy, and Brunauer–Emmett–Teller methods. To investigate the composition of the particles in the sample, such methods as Fourier transform infrared spectroscopy, Raman spectroscopy, differential scanning calorimetry, and X-ray diffraction, were applied. Magnetite phase was found to be sufficiently pure, it was not contaminated by other iron oxide phases and contained not more than 0.5% of metallic iron in form of large particles. The study of the magnetic properties of the magnetite nanoparticles obtained has shown that they exhibit ferrimagnetic behavior at room temperature with the paramagnetic contribution explained by the presence of fine superparamagnetic particles.

Keywords Magnetite · Pulsed laser ablation · Nanoparticles · Dispersion

✉ A. V. Shabalina
shabalinaav@gmail.com

[1] Tomsk State University, Lenina ave., 36, Tomsk 634050, Russia

[2] Kirensky Institute of Physics, Federal Research Center KSC SB RAS, Akademgorodok 50, bld. 38, Krasnoyarsk 660036, Russia

1 Introduction

Magnetite particles less than 30 nm in diameter may exhibit phenomena such as enhanced coercivity, reduced saturation magnetization and superparamagnetism at room temperature [1, 2]. Concerning biomedicine, magnetic nanoparticles with such specific properties have found their application in imaging, diagnostics, magnetic separation, drug delivery, and therapy [3–11]. A wide variety of synthetic methods allows the obtainment of iron oxide nanoparticles, including magnetite. The list of the methods embraces co-precipitation, modified with different accompanying techniques (hydrothermal treatment, for example [12, 13]), inert gas condensation [2], electrochemical synthesis [14], and others. Among them, pulsed laser ablation in liquids (PLAL) is one of the most convenient, simple, fast, low-cost methods, and it is easy to control the processing parameters. It allows the obtainment of stable nanoparticle dispersions in different liquids even without the addition of surfactants and stabilizers, which is quite desirable for biomedicine applications [15].

Pandey et al. performed pulsed laser ablation of industrial hematite powder in water and surfactant solution, which resulted in powder restructuring and enhancement of its magnetic and other properties [16]. Maneeratanasarn and co-authors found that iron oxide powder ablation in different solvents (water, ethanol, and acetone) resulted in hematite and maghemite formation [17]. They concluded that obtaining magnetite requires more powerful laser radiation. Metallic iron powder was exposed to ablation in liquids as well [18]. Laser radiation both in the UV and in visible ranges resulted in obtaining only hematite particles of different shapes. Thus, magnetite does not normally form via ablation of iron powder or its oxide powders in liquids.

Metallic iron target is also used to obtain iron oxides via ablation in liquids. De Bonis et al. obtained FeO and Fe_3O_4 in water and acetone from Fe target and indicated that the thermal properties of the solvent were crucial [19]. Wustite alone was obtained by the ablation of Fe target in ethanol and acetone, but in water, the ablation products were FeO and Fe_2O_3 [20]. Sukhov et al. prepared core–shell structures with the metallic core covered with iron oxides, including magnetite [21]. Omelchenko et al. obtained metallic core-magnetite shell nanoparticles covered with polyvinylpyrrolidone [22]. In the work of Iwamoto and Ishigaki, three different targets were treated in water by laser: Fe, Fe_2O_3, and Fe_3O_4. In all cases, wustite and magnetite were obtained, and Fe and Fe_2O_3 appeared in the products depending on the target [23]. Thus, pulsed laser ablation of Fe target in pure water leads more often to the formation of metallic iron and/or a mixture of its oxides [24]. Thereby, obtaining pure magnetite nanoparticles via pulsed laser ablation in water without additives and stabilizers is an interesting and challenging task. In the present work, we obtained magnetite nanoparticles in form of the stable water dispersion via PLAL and investigated their composition, structure, and magnetic properties.

2 Experimental

Dispersion of nanoparticles (concentration of 0.2–0.3 g/l) was obtained using focused radiation of Nd:YAG laser TII LS-2131M-20 (LOTIS, Belarus) at 1064 nm, 20 Hz, 7 ns, and 150 mJ. The experimental conditions of PLAL were described in detail in our previous work [25]. The laser radiation was focused by a short-focus lens ($F = 50$ mm). Laser beam was introduced into the reactor through the sidewall of the glass. This focusing technique allows controlling the power density on the target surface during ablation. In the present work, the power density was about 600 MW/cm^2. A layer of the liquid in front of the target did not exceed 5 mm. Short-focus lens, minimal thickness of the liquid layer in front of the target, irradiation wavelength in IR region, and pulse duration of few nanoseconds minimized the secondary effects of interaction between the nanoparticles and laser radiation in the colloid. The pulse duration used also provided a sufficient intensity of radiation for the effective synthesis of particles with the formation of a minimum fraction of the melted phase during ablation. The concentration of obtained dispersion was assessed by the weight loss of the target.

The zeta potential of the particles in their dispersion was measured on Omni S/N (Brookhaven, USA) in ZetaPALS mode with a BI-ZTU autotitrator (Brookhaven, USA) for changing the pH; the previously described method was used [26]. During the analysis, the pH was adjusted using diluted solutions of KOH and HNO_3 (10^{-1} to 10^{-3} M). The ionic concentration was maintained with 10^{-2} M KNO_3 as a background electrolyte. Average values from three measurements were used.

Microscopic investigations were conducted on a Hitachi TEM System (Hitachi, Japan) at 110 kV, and with a scanning electron microscope Vega 3 SBH (Tescan, Czech Republic) at 20 kV.

Transmission electron microscopy (TEM) images were obtained for colloid dripped onto carbon-coated copper grids and dried. Scanning electron microscopy (SEM) images were recorded for the powder sample applied to carbon conductive adhesive. Particles size distribution as a histogram of a relation between particles diameter and their amount was obtained by the measurement of 2000 particles diameter manually. Five HR TEM images with the scale bar of 20 nm were treated for this.

Brunauer–Emmett–Teller (BET) surface area value and pore size distribution were obtained using a gas-adsorption analyzer of specific surface and porosity, TriStar II 3020 (Micromeritics, USA). Before analysis, the powder samples of the material were degassed in a vacuum (10^{-2} Torr) at 200 °C for 2 h. Pore size distribution and porosity were calculated based on a desorption isotherm using the Barrett–Joyner–Halenda (BJH) method.

X-ray diffraction (XRD) patterns were obtained using an XRD 6000 diffractometer (Shimadzu, Japan). Phase identification was conducted with the data from the PDF-4 database. Calculations were performed using Powder Cell 2.4 (Germany). Differential scanning calorimetry (DSC) data was obtained using DSC 204F1 Phoenix (Netzsch, Germany). A powder sample of 17.5 mg in an Al crucible was heated from 25 to 600 °C at a rate of 2 °C/min in air. Fourier transform infrared spectroscopy (FTIR) spectra were obtained on the TENZOR 27 (Bruker, Germany) spectrometer. Raman spectra of the powder obtained were recorded using the Raman microscope InVia (Renishaw, UK) at an excitation of semiconductor laser (wavelength of 785 nm, CW power of 100 mW) and 50× objective. The maximum laser intensity at the sample surface under focusing achieved 250 kW/cm^2.

Magnetic properties of the material obtained were investigated using a vibrating sample and SQUID magnetometers in a magnetic field up to ± 20 kOe. An electromagnet with high uniformity of magnetic field at the sample was used as a source. The temperature was varied from 4 to 300 K by flow cryostat. Magnetic measurements were carried out using a direct method of measuring the inductive electromotive force. Mechanical vibrations of the sample were provided by a vibrator of the original design. The relative instability of the oscillation amplitude was 0.01% with a frequency of 0.001%. Registration of the signal was conducted using the system of four pickup coils. The dynamic range of the

device was 5×10^{-6}–100 emu. The working principle and design of the magnetometer are described in detail in [27]. The investigated nanoparticle powder was ground with KBr powder and pressed into a tablet for magnetic measurements.

3 Results and discussion

3.1 Investigation of the structure of the particles obtained

The zeta potential of the nanoparticles in the water dispersion after preparation was found to be 24.2 mV, and the isoelectric point was around 7.5; the pH of the dispersion was 5.85. So, the nanoparticles in the dispersion were characterized by a surface charge and thus electrostatic stabilization [28], and did not require additives of surfactants and stabilizers. The stability of the dispersion is a very important factor, as in the case of using of magnetic nanoparticles for biomedical applications, their dispersion has to be stable without any additional stabilizing agents.

After vacuum drying, the powder from the dispersion was studied by SEM. SEM images obtained by collection of secondary and back-scattered electrons are presented in Fig. 1. It can be seen that the powder consisted of agglomerates of small particles. These agglomerates formed a porous structure. Z-contrast (Fig. 1, right image) shown that the distribution of elements in the sample was relatively homogenous, but there were brighter spherical pieces that might contain more metallic iron than the rest of the sample. It was suggested that these particles were large pieces of metallic target that may have not oxidized completely.

The TEM images of the nanoparticles obtained are presented in Fig. 2. It is seen that the particles are agglomerated that either is the effect of drying of the dispersion during sample preparation to TEM examination, or they might originally be present in such agglomerates in the dispersion. The size of agglomerates can reach few micrometers.

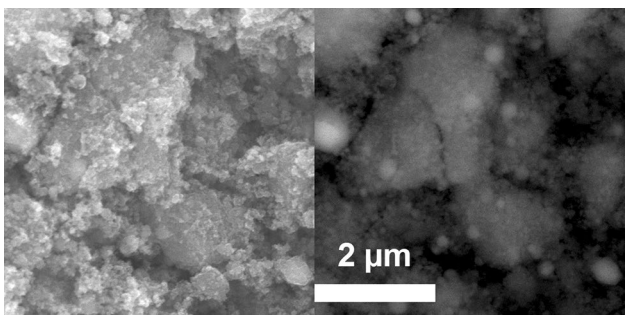

Fig. 1 SEM images of the powder prepared by drying the water dispersion of nanoparticles obtained by PLAL. Secondary electrons detected (left) and back-scattered electrons detected, z-contrast (right)

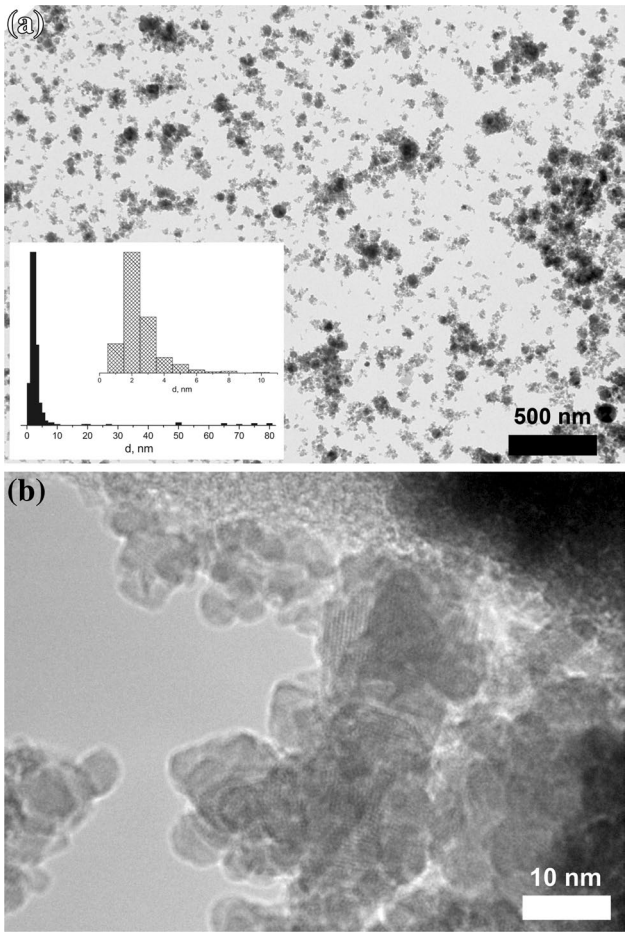

Fig. 2 Different magnifications (**a** and **b**) of TEM images of iron oxide nanoparticles from water dispersion obtained by PLAL. Inset in (**a**): nanoparticle size distributions for the ranges 0–80 nm and 0–10 nm, obtained for 2000 particles from five HR TEM-images

Large (up to 80 nm) spherical particles are surrounded by smaller near-spherical and faceted particles (1–10 nm). Particle size distributions were obtained for both wide range (0–80 nm) and the finest fraction (0–10 nm) because the majority of particles were collected in very dense agglomerates and had a size up to 10 nm. The inset of Fig. 2a provides a histogram indicating that the maximum of the particle size distribution was at 2 nm. A high-resolution TEM (HRTEM) image in Fig. 2b shows an interplanar distance of 4.87 Å that is in agreement (taking the error into account) with that of both the (011) plane of magnetite and the (111) plane of maghemite. This was not enough to determine the phase composition of the sample.

The S_{BET} of the powder was found to be 120 m^2/g, with a general pore volume of 0.21 cm^3/g (BET data are presented in Fig. 3). The pore size distribution was bimodal (Fig. 3b) with the maxima at 3.5 and 6.5 nm, and the average calculated pore diameter was 6.9 nm. This is consistent

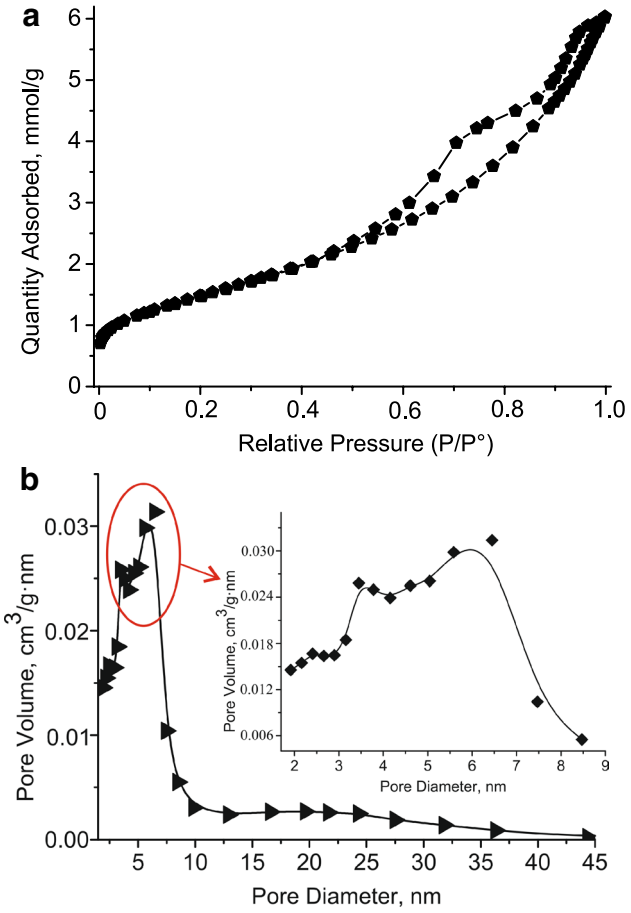

Fig. 3 BET data for the nanoparticles obtained by PLAL of Fe target in water: **a** adsorption–desorption curve, **b** pore size distribution

with the results from TEM and SEM: very small particles formed quite dense agglomerates.

3.2 Investigation of the composition of the particles obtained

XRD data are presented in Fig. 4. It can be seen that the main signals of magnetite and hematite overlap (2θ of 30, 37, 42, 57, and 63°), and all of them can be found in the resulted XRD pattern for the powder obtained after drying the dispersion of iron oxide nanoparticles. It has already been announced that the distinguishing between iron oxide phases is not an easy task, and XRD data are not applicable for this purpose [29]. Thus, to establish the real composition of the sample, other physical–chemical methods were used. However, the mean size of coherent scattering regions for this total oxide phase was calculated to be around 10 nm. Additionally, three peaks of metallic Fe (at 45, 65, and 83°) still can be recognized in the diffractogram, which may belong to the large particles (tens of nm) that are seen on SEM images (Fig. 1). The calculation results indicated

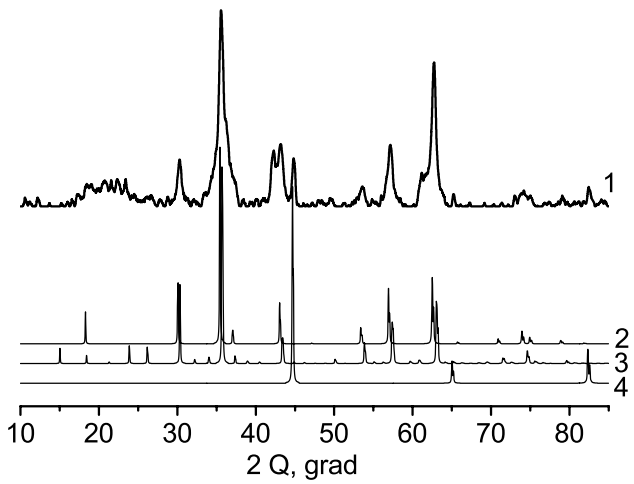

Fig. 4 Diffraction patterns for (1) the powder of the sample obtained by PLAL, (2) for Fe_3O_4 (#04-013-7114), (3) Fe_2O_3 (#01-078-6916), (4) Fe (#01-071-4648)

that only 0.5% of this phase in the sample present with the minimum size of coherent scattering regions of 20 nm. It should be noted that these large metal particles can be easily separated using standard methods (e.g., centrifugation).

DSC data are presented in Fig. 5. Water loss was observed at ~ 100 °C (the first endothermic peak). More transitions were seen on the DSC curve and derivative graph. According to the literature, exothermic processes at 200–270 °C belong to the magnetite→maghemite transition, and the transformation at 460 °C is γ→α conversion of Fe_2O_3 [30, 31]. Thus, DSC data indicated that the main phase of the powder obtained from the ablated dispersion was Fe_3O_4. There were no signals of metallic Fe oxidation. This can be explained by the amount of the sample that is used for the

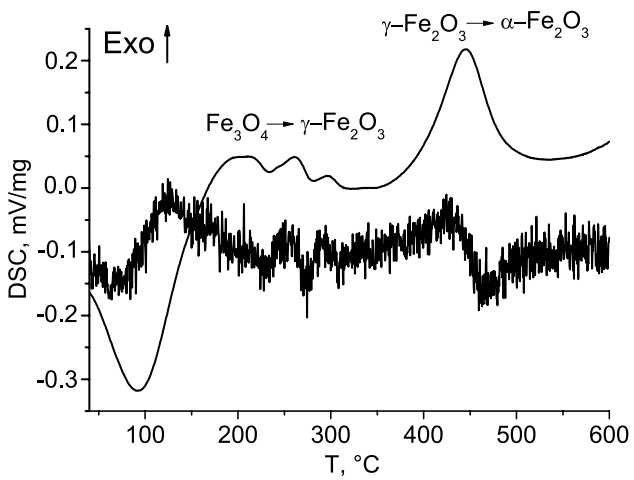

Fig. 5 DSC curve and its derivative obtained for the nanoparticles from the dispersion obtained by PLAL of Fe target in water

analysis. XRD requires approximately 0.5 g of the powder, whereas 5–10 mg is normally used for DSC measurements. As the Fe phase was less than 1% of the sample under study, the signal was inconsequential in this case.

The FTIR spectrum of the powder obtained is presented on Fig. 6. Bands at 437, 456, 553 cm^{-1}, and a shoulder at 481 cm^{-1} belong to Fe_3O_4 [22]. The bands at 553 and 437 cm^{-1} may be metal–oxygen bands corresponding to the intrinsic stretching of the tetrahedral and octahedral sites of the inverse spinel cubic of Fe_3O_4, respectively [22]. The bands at 553 and 684 cm^{-1} are also of the stretching vibrations of Fe–O in Fe_2O_3.[16] O–H stretching and deformation vibrations of absorbed water are presented by bands at 1050, 1345, 1467, 1619, and around 3200 cm^{-1} [16, 22]. Thus, there are likely magnetite nanoparticles in the powder obtained, and they may be mixed with maghemite or hematite.

The Raman spectra of the nanoparticles obtained by PLAL are presented in Fig. 7. The spectra recording was performed according to the next scheme. The sample was placed into the Raman spectrometer. The first spectrum was recorded at the low power of a semiconductor laser of the spectrometer (curve 1). This low power was of 0.5%, and the power density at the sample was 1.25 kW/cm^2. After that, the sample was purposely irradiated by the spectrometer laser with the power density of 2.5 kW/cm^2 for 50 s. Then, the second spectrum was recorded (curve 2). Later, the sample was irradiated again with the higher power density (12.5 kW/cm^2) for 50 s, and the third spectrum was recorded for this irradiated sample (curve 3). The last irradiation for

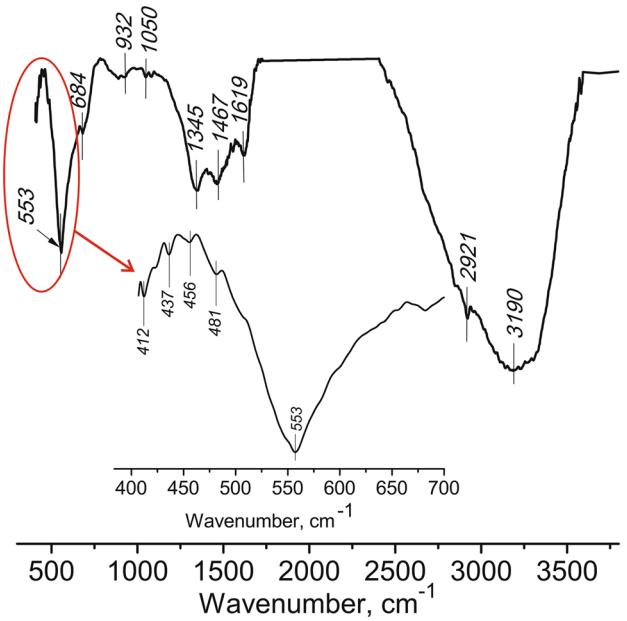

Fig. 6 FTIR spectrum of the powdered nanoparticles obtained via PLAL with the fragment for 400–600 cm^{-1} enlarged

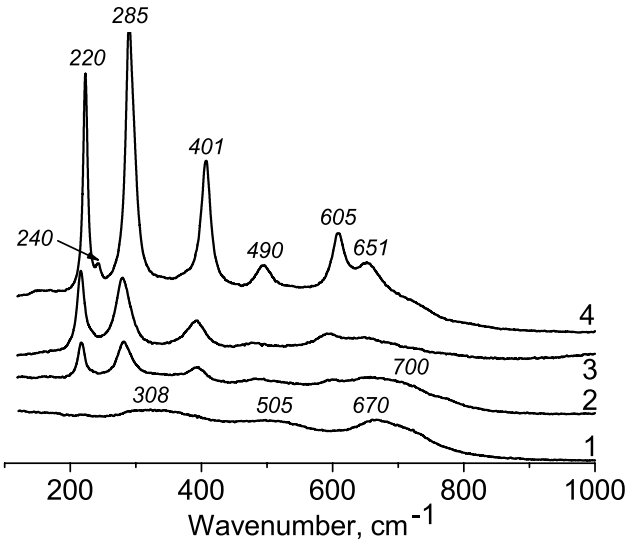

Fig. 7 Raman spectra of the powder prepared by drying the dispersion obtained by pulsed laser ablation of Fe target in water: before (curve 1) and after 50 s of irradiation with the power of 2.5, 12.5, and 25 kW/cm^2 (bottom up, curves 2–4)

50 s was performed at the power density on the sample of 25 kW/cm^2. The fourth curve was obtained for the sample after this last irradiation. So, the sample was treated by laser of the Raman spectrometer, and the spectra were recorded for each irradiation step.

In the first spectrum, a characteristic band of magnetite around 670 cm^{-1} can be clearly seen [32]. Additionally, a weak, broad band around 308 cm^{-1} may be identified as belonging to Fe_3O_4. Shebanova and Lazor assigned the bands obtained for a magnetite crystal as follows: 668(a_{1g}), 538 (T_{2a}), and 306(e_g) [33]. Thus, in the initial state, the sample obtained in this work by PLAL consists of magnetite only.

It was announced that under high-power laser radiation, the magnetite is transformed to a hematite/maghemite mixture [33]. This is why an experiment with consistent increases in laser power was conducted. It can be seen that the second curve (after 2.5 kW/cm^2 laser exposure) differs from the first one. The magnetite bands almost completely disappeared, and two bands at approximately 210 and 280 cm^{-1} that belong to hematite came into sight. The following irradiation (with the laser power density of 12.5 kW/cm^2, curve 3) led to these bands increasing and three more signals' appearance. The bands at 700, 500, and 360 cm^{-1} are characteristic for maghemite [32, 34].

Then, after the subsequent irradiation (25 kW/cm^2, curve 4), the most pronounced peaks formed. Almost all the bands in this spectrum are attributed to hematite: 605 (e_g), 491 (a_{1g}), 401 (e_g), 285 (e_g), 240 (e_g), and 220 (a_{1g}) cm^{-1}. The band at 651 cm^{-1} belongs to maghemite (a_{1g}). Thus, magnetite under laser powerful radiation transforms to hematite

but via the stage of maghemite formation. This is consistent with previously published data that the transformation of powder of magnetite into hematite occurs via a metastable maghemite formation [32–34].

Thus, the dispersion of nanoparticles obtained via pulsed laser ablation of iron target in water and the powder obtained by the drying of the dispersion consisted of fine magnetite particles and contained larger metallic iron particles of no more than 0.5%.

3.3 Investigation of magnetic properties of nanoparticles obtained

Figure 8 shows the magnetization curves obtained in an external magnetic field from 0 to 20 kOe both in a positive and negative direction.

The shape of the magnetization loops was characteristic for either ferrimagnetic or ferromagnetic particles. As can be seen, the saturation magnetization and coercivity increase with the decrease in temperature. This indicates the possible heterogeneity of the magnetic structure and ferromagnetic correlations in the sample. According to the data obtained, there are at least two magnetic contributions in the material: paramagnetic and ferromagnetic or ferrimagnetic. This may be caused by the relatively wide particle size distribution. Probably, the sample consisted of two kinds of nanoparticles: one was in a superparamagnetic state, and the rest were ferrimagnetic. Additional temperature-dependent measurements of magnetization in a weak magnetic field are needed to prove this assumption.

When the temperature was lowered to 77 K, an increase in the coercive field from 144 Oe to 370 Oe took place, and an increase in the magnetization that was near saturation by 20% was observed (that is also typical for ferromagnets). The fact that the hysteresis curves did not reach the saturation in the measured field range may be explained by the paramagnetic contribution. This may be due to the presence of superparamagnetic fine particles, or it can be caused by temperature fluctuations of the magnetic moment orientation.

The temperature-dependent magnetic properties of the powder obtained were investigated using the SQUID magnetometer. Two modes were performed. Zero field-cooling (ZFC) mode consisted of the sample cooling to 4 K in a zero magnetic field with the subsequent heating up to 300 K in the constant field and the sample magnetization measurements. Then, the sample was cooled at the constant magnetic field–field-cooling (FC), and the corresponding measurements during heating were performed. The temperature dependence of the magnetization in FC and ZFC modes at 200 Oe is shown in Fig. 9.

In the given field, the FC and ZFC curves did not coincide. The behavior of the ZFC curve was typical for superparamagnetic particles [35]. The Verwey transition that is characteristic for magnetite did not appear at the ZFC curve, which may be explained by the very small particle size (or crystalline domains of the larger particles) in the sample [36, 37]. The wide maximum at the ZFC curve was centered around room temperature, indicating the presence of not only the fine fraction in the sample but also the larger particles [37]. Normally, the maximum at the ZFC curve corresponds to a blocking temperature T_b, and it is characterized by the most probable particle size in the sample [38]. The point of the FC and ZFC curves separation corresponds to a temperature of irreversibility (T_{irr}), and it is the blocking temperature of the largest particles of the sample. The difference between these two characteristic temperatures might be considered as a quantitative measure of the particles size distribution. In the case under study, T_b was found at ~230 K,

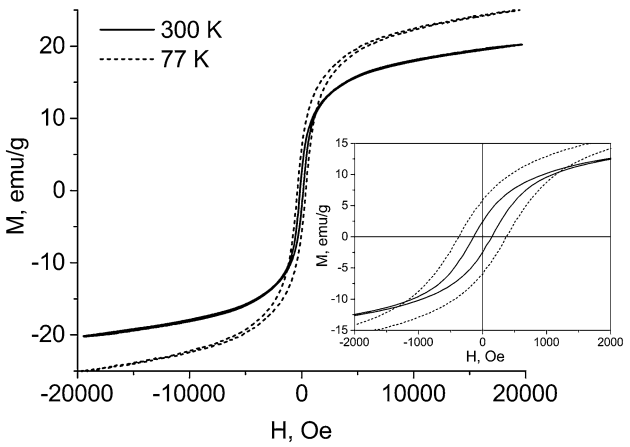

Fig. 8 Hysteresis loops for Fe_3O_4 nanoparticles in KBr tablet at 77 and 300 K

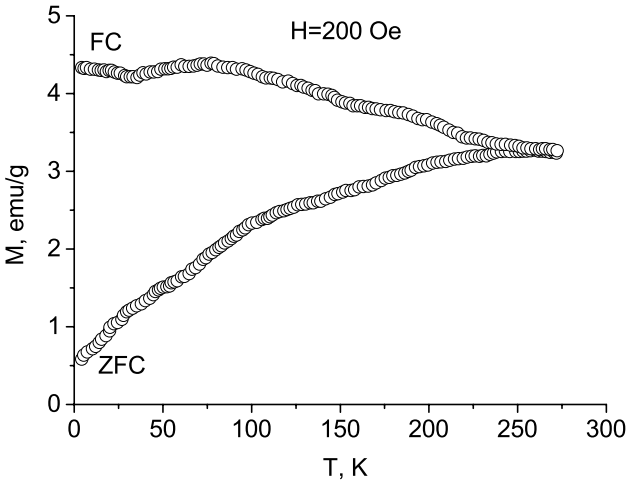

Fig. 9 FC and ZFC curves of Fe_3O_4 sample in the field of 200 Oe

and T_{irr} was at 280 K that belonged to large particles size distribution and was confirmed by the microscopic data.

Overall blocking temperature around room temperature indicated that the particles in normal conditions were blocked. As it was mentioned above, hysteresis curves without saturation in the measured field range may be explained by the presence of superparamagnetic fine particles or temperature fluctuations in the magnetic moment orientation. Because below T_b, the temperature fluctuations of magnetic moments are blocked under the influence of magnetic anisotropy [39], the presence of fine supermaramagnetic particles in the sample is more probable.

The temperature dependence of the magnetization in the field of 10 kOe is presented in Fig. 10. In the case of the strong magnetic field, the hysteresis loop was absent, and the FC and ZFC curves coincided. Thus, the resultant curve was actually the graph for the dependence of saturation magnetization (M_s) on temperature. For ferromagnetic materials, this dependence obeys the Bloch law $T^{3/2}$ [37].

At the same time, for the small clusters (nanoparticles) present in the sample (as discussed above), the index of the T-parameter in the equation can increase. The possibility of its change in the region from 3/2 to 3 for different particle sizes was shown [39]. In this work, the approximation of the experimental curve in the saturation field in accordance with the Bloch law led to the following fitting parameters: $M_0 = 22.28$ emu/g and $\alpha = 2.02$.

Using this approximation, a Curie temperature for the particles was estimated, $T_c(M_s=0) \approx 600$ K. Using the molar mass value of the nanoparticle formula unit, one can estimate the magnetic moment per one formula unit, $M^{Fe}=0.31$ μB. It is approximately ten times lower than the magnetic moment of bulk magnetite [40]. Apparently, such a low value of the magnetic moment can be explained by the difference between contributions of surface and bulk atoms.

Thus, it was found that the particles are ferrimagnetic at room temperature, but the paramagnetic contribution also occurred. It was suggested that this contribution can be explained by the presence of fine superparamagnetic particles. A high blocking temperature value indicates the blocked state of the particles at room temperature.

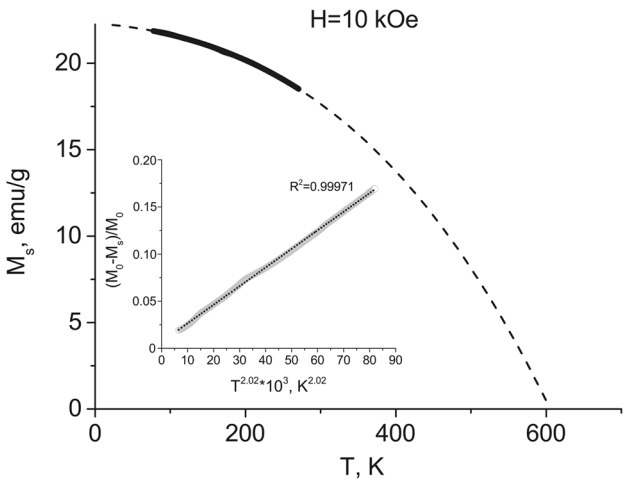

Fig. 10 The temperature dependence of the saturation magnetization (FC and ZFC modes) of the Fe_3O_4 sample in the field of 10 kOe: bold is for the experimental data, and dashed is for an approximation with $T^{2.02}$. Inset: linearization of the Bloch law curve with obtained fitting parameters

4 Conclusion

Fine magnetite nanoparticles were obtained via pulsed laser ablation in liquid. The particles are synthesized in the form of stable water dispersion without the introduction of additional components such as stabilizers and surfactants that allow the use of this material in biomedicine. Magnetite was found to be sufficiently pure from the other oxide phases; the only contamination was 0.5% of metallic iron larger particles (up to 80 nm).

The results of the investigation of magnetic properties indicated that Fe_3O_4 nanoparticles have a complex magnetic ordering. Large magnetic particle size distribution was revealed, that coincided with the microscopic data. Magnetic behavior of the particles can find application in such biomedical applications as magnetically controlled drug delivery, magnetic separation, magnetic-mediated hyperthermia, and so on.

The colloidal solutions of magnetite nanoparticles obtained in the work and their magnetic, dimensional and other characteristics will be used for applications in medicine and biology. Our further research will be aimed at creating complex composite nanostructures based on magnetite nanoparticles (for example, magnetite-gold, magnetite-DNA aptamers and magnetite-gold-DNA aptamers compositions) for anticancer therapy and diagnostics.

Acknowledgements This work was conducted as a government task of the Ministry of Education and Science of the Russian Federation, Project Number 3.9604.2017/8.9.

References

1. E. Vahabzadeh, M. Torkamany, J. Cluster Sci. **25**, 959 (2014)
2. C. Baker, S. Ismat Shah, S.K. Hasanain, J. Magn. Magn. Mater. **280**, 412 (2004)
3. C. Wen, H. Xie, Z. Zhang, L. Wu, J. Hu, M. Tang, M. Wu, D. Pang, Nanoscale **8**, 12406 (2016)
4. O. Penon, M.J. Marin, D.B. Amabilino, D.A. Russell, L. Perez-Garcia, J. Colloid Interface Sci. **462**, 154 (2016)
5. J. Zhang, N. Chen, H. Wang, W. Gu, K. Liu, P. Ai, C. Yan, L. Ye, J. Colloid Interface Sci. **469**, 86 (2016)

6. H. Liu, J. Zhang, X. Chen, X. Du, J. Zhang, G. Liu, W. Zhang, Nanoscale **8**, 7808 (2016)
7. S. Yu, J. Wan, K.A. Chen, J. Colloid Interface Sci. **461**, 173 (2016)
8. D. Xu, T. Xu, X. Guo, Q. Liu, J. Liu, W. Lv, X. Jing, H. Zhang, J. Wang, New J. Chem. **41**, 5305 (2017)
9. K. Wu, J.P. Wang, AIP Adv. **7**, 056327 (2017)
10. M. Qi, K. Zhang, S. Li, J. Wu, C. Pham-Huy, X. Diao, D. Xiao, H. He, New J. Chem. **40**, 4480 (2016)
11. W. Wu, C. Jiang, V.A.L. Roy, Nanoscale **8**, 19421 (2016)
12. C. Sciancalepore, F. Bondioli, T. Manfredini, A. Gualtieri, Mater. Charact. **100**, 88 (2014)
13. S.G. Mendo, A.F. Alves, L.P. Ferreira, M.M. Cruz, M.H. Mendonca, M. Godinho, M.D. Carvalho, New J. Chem. **39**, 7182 (2015)
14. M. Aghazadeh, I. Karimzadeh, T. Doroudi, M.R. Ganjali, P.H. Kolivand, D. Gharailou, Appl. Phys. A **123**, 529 (2017)
15. G.W. Yang, Prog. Mater. Sci **52**, 648 (2007)
16. B.K. Pandey, A.K. Shahi, J. Shah, R.K. Kotnala, R. Gopal, Appl. Surf. Sci. **289**, 462 (2014)
17. P. Maneeratanasarn, T.V. Khai, S.Y. Kim, B.G. Choi, K.B. Shim, Phys. Status Solidi A **210**, 563 (2013)
18. S. Mollah, S.J. Henley, C.E. Giusca, S.R.P. Silva, Integr. Ferroelectr. **119**, 45 (2010)
19. T. De Bonis, A. Lovaglio, A. Galasso, R. Santagata, Teghil, Appl. Surf. Sci. **353**, 433 (2015)
20. H.L. Aye, S. Choopun, T. Chairuangsri, J. Nat. Sci. **13**, 37 (2014)
21. I.A. Sukhov, A.V. Simakin, G.A. Shafeev, G. Viau, C. Garcia, Quantum Electron **42**, 453 (2012)
22. A.I. Omelchenko, E.N. Sobol, A.V. Simakin, A.A. Serkov, I.A. Sukhov, G.A. Shafeev, Laser Phys. **25**, 025607 (2015)
23. T. Iwamoto, T. Ishigaki, J. Phys. Conf. Ser. **441**, 012034 (2013)
24. E. Vahabzadeh, M.J. Torkamany, J. Cluster Sci. **25**, 959 (2014)
25. V.A. Svetlichnyi, A.V. Shabalina, I.N. Lapin, Russ. Phys. J. **59**(12), 2012 (2017)
26. C.C.P. Chan, H. Gallard, P. Majewski, J. Nanopart. Res. **14**, 828 (2012)
27. D.A. Velikanov, Vibration Magnetic Meter, RU Pat. 2341810 (2008)
28. D. Zhang, B. Gokce, S. Barcikowski, Chem. Rev. **117**, 3990 (2017)
29. S. Das, M.J. Hendry, Chem. Geol. **290**, 101 (2011)
30. D.L.A. De Faria, S. Venancio Silva, M.T. De Oliveira, J. Raman Spectrosc. **28**, 873 (1997)
31. M. Aliahmad, N. Nasiri Moghaddam, Mater. Sci. Pol. **31**, 264 (2013)
32. Y.S. Li, J.S. Church, A.L. Woodhead, J. Magn. Magn. Mater. **324**, 1543 (2012)
33. O.N. Shebanova, P. Lazor, J. Solid State Chem. **174**, 424 (2003)
34. O.N. Shebanova, P. Lazor, J. Raman Spectrosc. **34**, 845 (2003)
35. O.S. Ivanova, I.S. Edelman, R.D. Ivantsov, E.A. Petrakovskaja, D.A. Velikanov, N.N. Trofimova, Y.V. Zubavichus, Solid State Phenom. **215**, 173 (2014)
36. V. Amendola, M. Meneghetti, G. Granozzi, S. Agnoli, S. Polizzi, P. Riello, A. Boscaini, C. Anselmi, G. Fracasso, M. Colombatti, C. Innocenti, D. Gatteschi, C. Sangregorio, J. Mater. Chem. **21**, 3803 (2011)
37. G.F. Goya, T.S. Berquo, F.C. Fonseca, M.P. Morales, J. Appl. Phys. **94**(5), 3520 (2003)
38. J. Lunacek, O. Zivotsky, Y. Jiraskova, J. Bursık, P. Janos, Mater. Charact. **120**, 295 (2016)
39. P.V. Hendriksen, S. Linderoth, P.A. Lindgard, J. Phys. Condens. Matter **5**, 5675 (1993)
40. E.W. Gorter, Philips Res Rep **9**(4), 295 (1954)